Carbon Trends 9 (2022) 100218

Contents lists available at ScienceDirect

Carbon Trends

journal homepage: www.elsevier.com/locate/cartre

Structural phase stability and homogeneity enhancement of electrochemically synthesized $Mn_2V_2O_7$ by nanocarbon networks

R. Parmar[a,b], S.J. Rezvani[b,c], D.B. de Freitas Neto[d], J.M. Rosolen[d], S. Kazim[b], S. Mattiello[b], P. Rajak[c], R. Ciancio[c], M.K. Thakur[e], M. Minicucci[b], M. Amati[a], L. Gregoratti[a], M. Kalbac[e], G. Haider[e], A. Di Cicco[b], R. Gunnella[b]

[a] Elettra-Sincrotrone, Strada Statale 14, AREA Science Park, Basovizza, 34149, Trieste, Italy
[b] Sez. Fisica, Scuola di Scienze e Tecnologie, Universitá di Camerino, via Madonna delle Carceri, Camerino I-62032, Italy
[c] CNR - Istituto Struttura della Materia and Elettra-Sincrotrone Trieste, Basovizza Area Science Park, Trieste 34149, Italy
[d] Universidade de São Paulo, Departamento de Química, Faculdade de Filosofia, Ciências e Letras de Ribeirão Preto, Avenida Bandeirantes 3900, Ribeirão Preto, 14040-901, SP, Brazil
[e] Department of Low-Dimensional Systems, J. Heyrovský Institute of Physical Chemistry, The Czech Academy of Sciences, Prague, Czech Republic

ARTICLE INFO

Article history:
Received 5 August 2022
Revised 8 September 2022
Accepted 19 September 2022

Keywords:
Polycrystalline $Mn_2V_2O_7$
Electrolytic graphene oxide
SPEM chemical mapping
Nanocarbon-MVO interaction

ABSTRACT

Structural phase stability and homogeneity of the electrochemically synthesized $Mn_2V_2O_7$ (MVO) on nanocarbon network structures are investigated. The cup-stacked multi-walled carbon nanotubes (CNTs) and electrolytic graphene oxide (eGO) are the networks exploited in present work. It is shown that co-electrodeposition of carbonaceous network and $V_2O_5.nH_2O$ followed by electro-insertion of Mn^{2+} cations results in the formation of intermixed β-$Mn_2V_2O_7$ nano-structures. The morphology and surface chemistry of the synthesized nano-structures is studied via high-resolution electron transmission and scanning X-ray photo-emission microscopies as well as Raman spectroscopy. The synthesized MVO on carbon fiber surface in the absence of the nanocarbon network shows a non-uniform phase formation and uneven coating distribution. The nanocarbon networks assisted MVO demonstrate uniform phase formation and distribution. The dominant MVO structural phase product present in these samples differs with different type of carbonaceous networks. The possible effect of the catalytic activity of the carbonaceous network as well as their hydrophilicity on the final structural and phase formation is discussed. The present study establishes new possibilities on catalytic assisted metal alloy oxide deposition for advanced applications.

1. Introduction

Vanadium oxide and manganese vanadium oxide (MVO) have been identified as a promising materials for advanced applications such as catalysts, battery electrodes, sensors and solar water splitting [1–9]. Several studies have been carried out for the synthesis of various manganese vanadium oxide phases with different structures and dimensions [10–17]. Out of these various phases the $Mn_2V_2O_7$ has shown promising properties to be employed in the renewable energy technology. The $Mn_2V_2O_7$ structure, also known as manganese pyrovanadate (formula of $A_2B_2O_7$, where A and B are divalent and pentavalent, respectively), shows a peculiar distorted honeycomb atomic arrangement. In the MVO structure, oxygen anions, manganese (Mn^{2+}) and vanadium (V^{5+}) cations occupy hexagonal closed packed sites, octahedral sites and tetrahedral sites in alternating parallel layers. MVO is composed with edge-sharing MnO_6^- octahedra, forming $(MnO_3)^-_n$ layers, which are shared with V_2O_7 (di-vanadate) groups on both sides of the honeycomb structure, producing a staggered configuration with a linear bridging VOV bonds [18]. β-/γ- $Mn_2V_2O_7$ phases (monoclinic systems (c2/m)) exhibit higher structural stability beyond 300 K temperature. Mn^{2+} cations in the β- $Mn_2V_2O_7$ phase consists of honeycomb layers separated by VO^-_4 groups pairwise bounded through bridging oxygen. The valence state of manganese may convert from Mn^{2+} to Mn^{3+}, which is an active state for oxygen reduction reaction (involving electron transportation) and contributes to catalysis, electrochemical energy storage and capacitive behavior. This makes the β-$Mn_2V_2O_7$ a potentially interesting material for solar water splitting applications [19]. However

E-mail addresses: rahul.parmar@elettra.eu (R. Parmar), sj.rezvani@unicam.it (S.J. Rezvani).

https://doi.org/10.1016/j.cartre.2022.100218

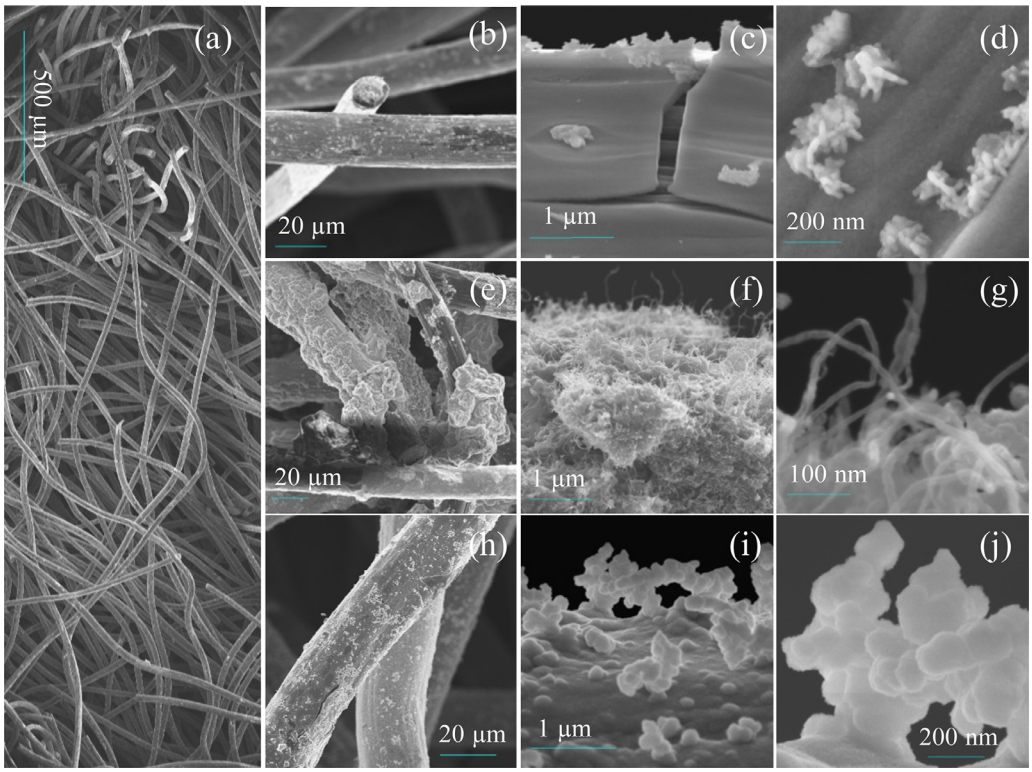

Fig. 1. Scanning electron microscope (SEM) of MVO deposited carbon fiber at low magnifications (a), MVO-CF (b-d), MVO-CNT (e-g), MVO-GO (h-j) at different magnifications.

the $Mn_2V_2O_7$ has shown structural instabilities, specially in electrochemical redox process where multivalent states of manganese ($Mn^{2+/3+}$) and vanadium ($V^{3+/4+/5+}$) cations occupy the octahedral and tetrahedral sites in a complex structure. On the other hand, most of the manganese and vanadium oxide based electrodes exhibit inherently poor electrical conductivity, which significantly reduces the electrochemical or photo-electrochemical devices performance. Hence, the integration of manganese vanadium oxide composite into the highly conductive carbonaceous networks such as graphene or carbon nanotube could significantly enhance the composite properties [20–23]. It has been shown that using multi-walled/single-walled CNTs can significantly improve the electrochemical performance of MVO based cathode material for multi-cations (i.e., Na^+/Zn^+) intercalation for batteries application [5,10]. The incorporation of CNTs with MVO expanded the interlayer lattice spacing of MVO that makes the MVO/CNTs composite more suitable to host large radius of cations into its crystal volume. The interlayer spacing along c-axis is strongly affected by the presence of water molecules between atomic bilayers of $Mn_xV_2O_5.nH_2O$, which can be intercalated during the synthesis in aqueous medium. The defective CNTs attract water molecules due to its hydrophilic characteristics which results to form a hydrated MVO structure. The discharge capacity of electrochemical device strongly depends on weight percentage (wt.%) of CNTs incorporation with metal oxide (Mn, V or Mn-V) nanostructures [10,20]. The stable discharge specific capacity of $\sim$ 400 mA h g^{-1} at a current density of 0.1 A g^{-1} have been reported for Na^+ and Zn^+ ion intercalation for MVO-CNTs composite for more than 100 charge-discharge cycles, which was calculated as comparatively high where the CNTs network was absent [5,10]. However, the phase formation mechanism and its correlation to the stability and distribution of MVO still remains unclear. In the present work, we have investigated the electrochemically synthesized MVO stable phases on the surface of carbonaceous network surface of CNTs, eGO and carbon fibers. The role played by the carbon network on the enhancement of the MVO phase formation and distribution is discussed.

2. Experimental

Electrochemical synthesis: Commercially available non-woven graphitic carbon fiber (CF) felt made from poly-acrylonitrile (PAN) was used as a substrate [24]. The CF substrate was cut into 7 mm diameter pieces of $\sim$ 3 mm thickness. The diameter range of single carbon fiber was from $\sim$ 10 to 25 µm. On the CF felt, cup-stacked type carbon nanotubes (CSCNTs) were grown by a chemical vapor deposition (CVD) method using a methanol precursor (carbon source), nitrogen gas as a carrier gas, a Co:Mn (1:1 wt. ratio) catalyst, and methanol solvent. The CSCNTs were grown at a temperature of 650 °C for 10 minutes in a tubular furnace. The GO was prepared using 0.1 M H_2SO_4 and flake graphite powder (50 mg) in an electrochemical reactor, where the graphite was attached to a stainless-steel plate (5 × 5 cm^2) using a slurry of graphite and 1% of carboxymethyl cellulose. The potential was applied between the graphite electrode and stainless-steel counter electrode (CE) during two hours of polarization at room temperature. The measured distance between the working electrode (WE) and CE was approximately 10 mm. To remove H_2SO_4, an anionic exchange column was used. Afterward, GO dispersion was performed in a dry in-room atmosphere to form a particulate material. For electrochemical deposition of vanadium oxide ($V_2O_5.nH_2O$) nanostructures, $VOSO_4.xH_2O$ powder (0.6 g) was dissolved into 60 ml 4:1 v:v ratio of DI-water (80%) and ethanol (20%) (pH = 4) to prepare the electrolyte solution. For co-electrodeposition of vanadium oxide ($V_2O_5.nH_2O$) and GO on CF, GO was added into $VOSO_4.xH_2O$, and an ethanol electrolyte (1.6 % of $VOSO_4.xH_2O$ wt.%) was used under magnetic agitation at an anodic potential of +4.0 mA for one hour [25,26]. After the electrochemical deposition of $V_2O_5.nH_2O$, the samples were

washed in deionized water and dry at 100 °C in vacuum oven. To follow the electro-insertion of Mn^{2+} cations into $V_2O_5.nH_2O$ structure, the samples were subjected to anodic polarization (+ 0.15 mA for one hour) into an electrolyte prepared with 0.25 mol/liter of $Mn(CH_3COOH)_2$ in DI-water (pH = 6), to achieve the final product of MVO on different nanocarbons network of eGO, CNTs and CF.

Structural characterization: Scanning Electron Microscopy (SEM) measurements were conducted on a ZEISS Gemini SIGMA 300 device at different magnifications. To confirm the presence of different MVO phases on the surface, Raman scattering (RS) was also performed. The Raman mapping was measured with a WiTec alpha300R spectrometer equipped with a piezo stage. An excitation laser wavelength of 532 nm and power of ∼ 1.0 mW were used. The laser was focused on the sample with a 50x objective lens on a spot with a diameter of around 500 nm. The spatially resolved Raman spectra were recorded using a 600 l/mm grating. Two spectral integrations times of 30 s were used for single spectra accumulation and mapping. Further details on the nanostructure were provided by high-resolution transmission electron microscopy (HRTEM) and selective area electron diffraction (SAED) using a JEOL 2010 UHR field emission gun microscope operated at 200 kV with a measured spherical aberration coefficient (Cs) value of 0.47 ± 0.01.For more detailed chemical analysis of the MVO thin film surface, Scanning Photoelectron Microscopy (SPEM) was performed at the ESCA Microscopy Beamline 2.2L in the Elettra synchrotron laboratory, Trieste, Italy. The SPEM approach has a high spatial resolution for characterizing the nanomaterials at a submicron scale, i.e., the X-ray photon beam is downsized to a submicron spot, and the sample surface is then mapped by scanning the sample with the focused beam. A beam diameter of 130 nm was obtained by using zone plate diffractive optics. The overall energy resolution was better than 200 meV. An X-ray photon energy calibration of 650.0 eV was performed by taking the Fermi-level energy. Photoelectrons were detected at a 60° angle with respect to the normal to the surface by using a 48-channel hemispherical analyzer electron detector. The samples were annealed at a 300 °C temperature inside the SPEM preparation chamber overnight under ultra-high vacuum (∼ 10^{-10} mbar) to remove any residual water or CO/CO_2 from the sample surface before the SPEM experiments.

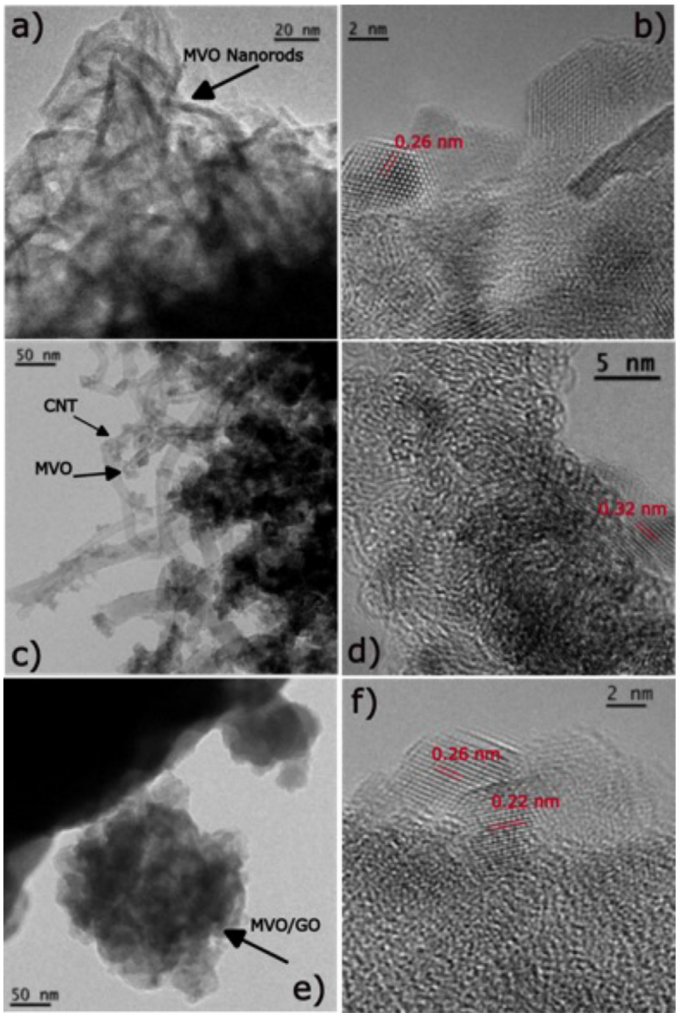

Fig. 2. HRTEM images of MVO samples: MVO-CF (a-b), MVO-CNT (c-d) and MVO-GO (e-f). The calculated MVO inter-planar distances for these three class of samples are shown in right hand side column images.

3. Results

Within the electrochemical deposition process, the MVO phase formation is expected to occur via the chemical reaction between vanadium oxide and manganese acetate as indicated in the nominal reaction below:

$$V_2O_5.0.5H_2O + 4Mn(CH_3COO)_2 \rightarrow Mn_2V_2O_7 + Mn_2O_3 + yCOOH^- + x.H_2O + \gamma.CO_2 \uparrow \quad (1)$$

In this process, the formation of manganese oxide and presence of the residual vanadium oxide can also be expected. The electrochemical synthesis of MVO was performed on three class of prepared substrates: the MVO on the carbon fibers (MVO-CF); MVO on carbon fibers covered by CNTs (MVO-CNT) and MVO with electrolytic graphene oxide on carbon fibers (MVO-GO). Surface morphologies of MVO-CF, MVO-CNT and MVO-GO samples are shown in Fig. 1. Low-magnification image shows the texture of non-woven type CF and the uniformity of electrochemical MVO growth over a large area. In SEM images, the non-woven type arrangement of MVO-covered CF surface can be seen in a diameter range from 20 to 30 μm. MVO on the CF surface shows nano-rods like-structures agglomerated in bunches on the surface (Fig. 1b-d). This sample also shows formation of cracks on the surface. The observed cracks in the MVO-CF sample surface is due the elastic stress at the hetero-junction interface as a results of the drying process after electrochemical deposition. It indicates a poor adhesion of MVO coating to the hydrophobic CF surface.

MVO on the CNTs network shows more uniform distribution in a crack free layer (see Fig. 1e-g). The MVO-CNT sample also shows a thicker deposited layers compared with the MVO-CF sample. The diameter of the CNTs was calculated to be in the range of ∼ 10 to 30 nm, in agreement with multi-wall cup-stacked carbon nanotubes, observed previously [21,27,28]. This type of CNT promote MVO growth on/between their non-woven matrix with higher surface adhesion and mechanical stability. On the other hand, the presence of GO in the electrolyte used for $V_2O_5.nH_2O$ co-electrodeposition, drastically alters the morphology of the resulting coatings (see Fig. 1h-j). MVO-GO sample demonstrate an altered texture with formation of nanoballs, packed on the surface of carbon fibers. MVO-GO nanoballs have diameters in the range of ∼ 100 to 300 nm. Crack formation in this sample is also negligible with a quasi uniform coverage of the fibers. In order to identify the crystallinity and atomic structure of the MVO on three different substrate class, TEM analysis was employed as shown in Fig. 2. The TEM images (Fig. 2a, e) show that MVO is grown as nanorods and nanoballs like shapes on the CF surface and with co-electrodeposited eGO, respectively. However, an intermixed growth of MVO was observed on the CNTs coated CF network (Fig. 2c) in agreement with the SEM analysis.

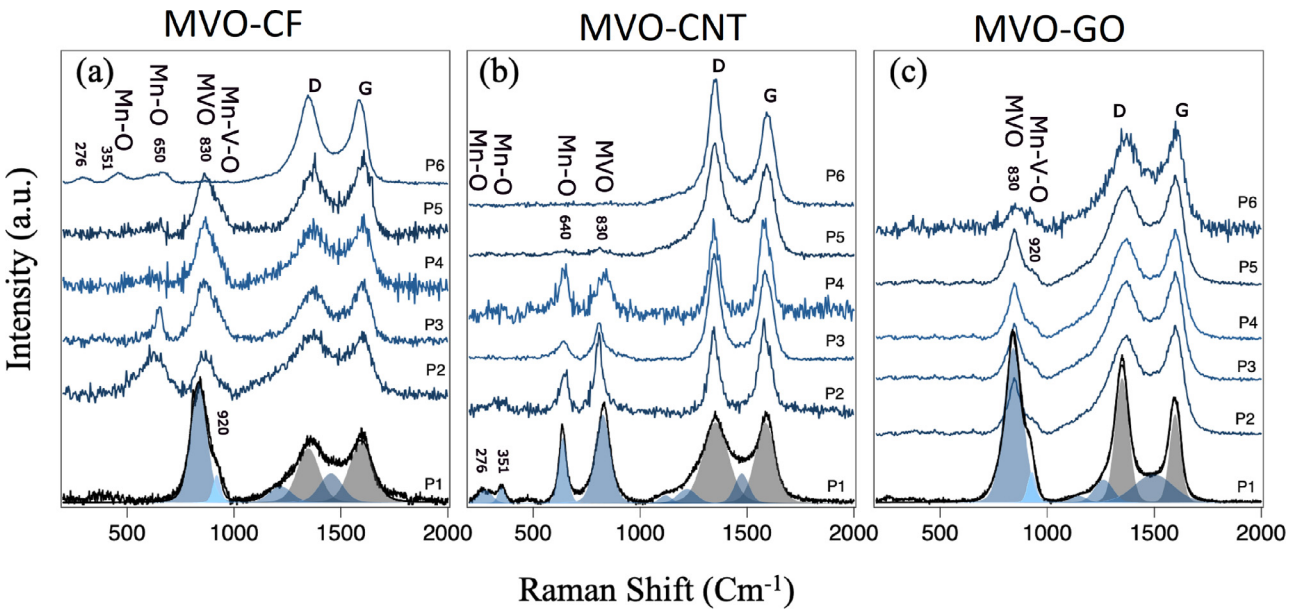

Fig. 3. The Raman spectra on the selected points of large area maps of (a) MVO-CF, (b) MVO-CNT, and (c) MVO-GO samples respectively. Each band has been marked and their corresponding peaks are assigned in each spectrum. All spectra are normalized with respect to G-band of carbon peak. The denoted points number from P1 to P6 are representing different positions on respective carbon fibers sample's surface.

Our results indicate that the MVO nanostructure appeared to have a polycrystalline structure in all the samples with various crystalline orientations. The MVO-CF and MVO-GO sample crystallizes in polycrystalline form with measured inter-planar distances of 0.22, 0.26 which corresponding to the (131), (220) crystallographic planes of β-$Mn_2V_2O_7$, respectively (JCPDS No. 22–043684 and 38-0034) [29–32]. The sample deposited on CNTs (MVO-CNT) shows a relatively larger inter-planar distance of about 0.32 nm correlating to the (021) crystallographic plane of the β-$Mn_2V_2O_7$. The MVO phases homogeneity on CF, CNTs, and eGO surfaces was investigated over a large area via spatially resolved micro-Raman scattering. Raman scattering microscopy were performed on the samples using a green laser (532 nm) and limited to $\sim$ 1 mW of power to avoid local laser heating and laser degradation and phase transition [33]. Fig. 3 show the selective Raman spectra at random positions (P1-P6) on the samples to check the uniformity and phase distribution.

Raman shifts at values of $\sim$ 276, 351 and $\sim$ 640 cm^{-1} can be correlated to the deformation/vibration of the Mn-O-Mn bonds (E_g mode), out-of-plane Mn-O bonds-bending vibrational modes (E_g mode) and Mn-O or Mn-O-Mn bonds asymmetric stretching vibrational modes (A_{1g} mode) in the layered Mn_2O_3 structure, respectively [34–36]. Shift in Mn_2O_3 vibrational modes can be due to cation-anion distortion or the presence of multiple oxidation states of Mn^+ in octahedral sites. On the other hand, the Raman shift at $\sim$ 830 cm^{-1} is assigned to Mn-V-O or V-O-Mn bridging bonds-stretching vibrational modes (mainly from $V^{5+/4+}$ and Mn^{2+} cations bonds with O^- anions) in the β-$Mn_2V_2O_7$ phase. The shoulder observed at around 920 cm^{-1} can be attributed to the O-V-O bonds stretching/bending vibration modes from secondary phase of $Mn_xV_2O_5$. Finally, the Raman shifts at $\sim$ 1350 and $\sim$ 1600 cm^{-1} are assigned to D- and G- carbon bands related to C-C defects like sp^3, out-of-plane C-C bonds vibration, chemical decoration in C-C rings (A_{1g} mode) and sp^2 C-C bond vibration along the plane (E_{2g} mode) in graphitic properties, respectively [37,38]. The additional components at $\sim$ 1120–1250 and 1450–1480 cm^{-1} are related to disordered amorphous rich carbon and to single bond C-H or C-O vibrations in hydrogenated/oxidized carbon [39–41]. The Raman spectra evidence existence of three different regions in the MVO-CF sample. A region with coexistence of β-$Mn_2V_2O_7$ and $Mn_xV_2O_5$, a region with dominance of MVO as well as presence of the manganese oxides and a third region in which there is only manganese oxide present. In the MVO-CNT sample Raman spectra have evidence of the homogeneous co-existence of Mn-O and MVO in the range of 500–1000 cm^{-1}. While in the MVO-CF sample, the predominance of MVO is evident but the lack of unique phase is absent. On the other hand, the MVO-CNT sample reveals only two regions. First, regions with the MVO and Mn-O co-existing on CNTs and second, regions where the fiber and CNTs are not covered with the MVO phase. The presence of the manganese oxides in this class of sample is predominant compared with the other two. Finally, the MVO-GO sample shows a relatively uniform distribution of the β-$Mn_2V_2O_7$ and $Mn_xV_2O_5$ through the sample. The manganese oxide phase is negligible compared with the MVO-CNT sample.

Phase distribution and stoichiometry at the surface of the samples were investigated using SPEM, rendering the analysis ultimately surface-sensitive. X-ray photoelectron spectroscopy maps acquired with SPEM, contain both topographic and chemical information (see Fig. 4). A topographic contribution removal approach was followed as detailed in reference article by Gregoratti et. al [42], to show the actual elemental distribution (i.e., chemical maps). Color contrast values represent the chemical state concentration on the sample surface in all SPEM maps. First column SPEM maps in Fig. 4 have been acquired at C-1s covering a large area to show the regions both coated and uncoated by MVO nanostructures. Then a selected areas (indicated by a square) was chosen where the both coated/uncoated regions were visible. Enlarged SPEM maps (C-1s, Mn-3p, and V-2p) were acquired for detailed chemical element distribution and phase analysis on the surface of samples. The enlarged chemical maps (Fig. 4b-d) at C-1s, Mn3p and V2p edges depict large manganese rich regions and small vanadium rich regions on MVO-CF sample surface. The manganese rich regions with low vanadium concentrations can correspond to manganese oxide phase (Mn_2O_3) dominance in the defined region. While the vanadium rich region with scarce Mn concentration can indicate the dominance of the $Mn_xV_2O_5$ phase with vanadium oxide prevalence. The MVO-CF samples shows a non-homogeneous distribution of the Mn and V over the sample surface which is in

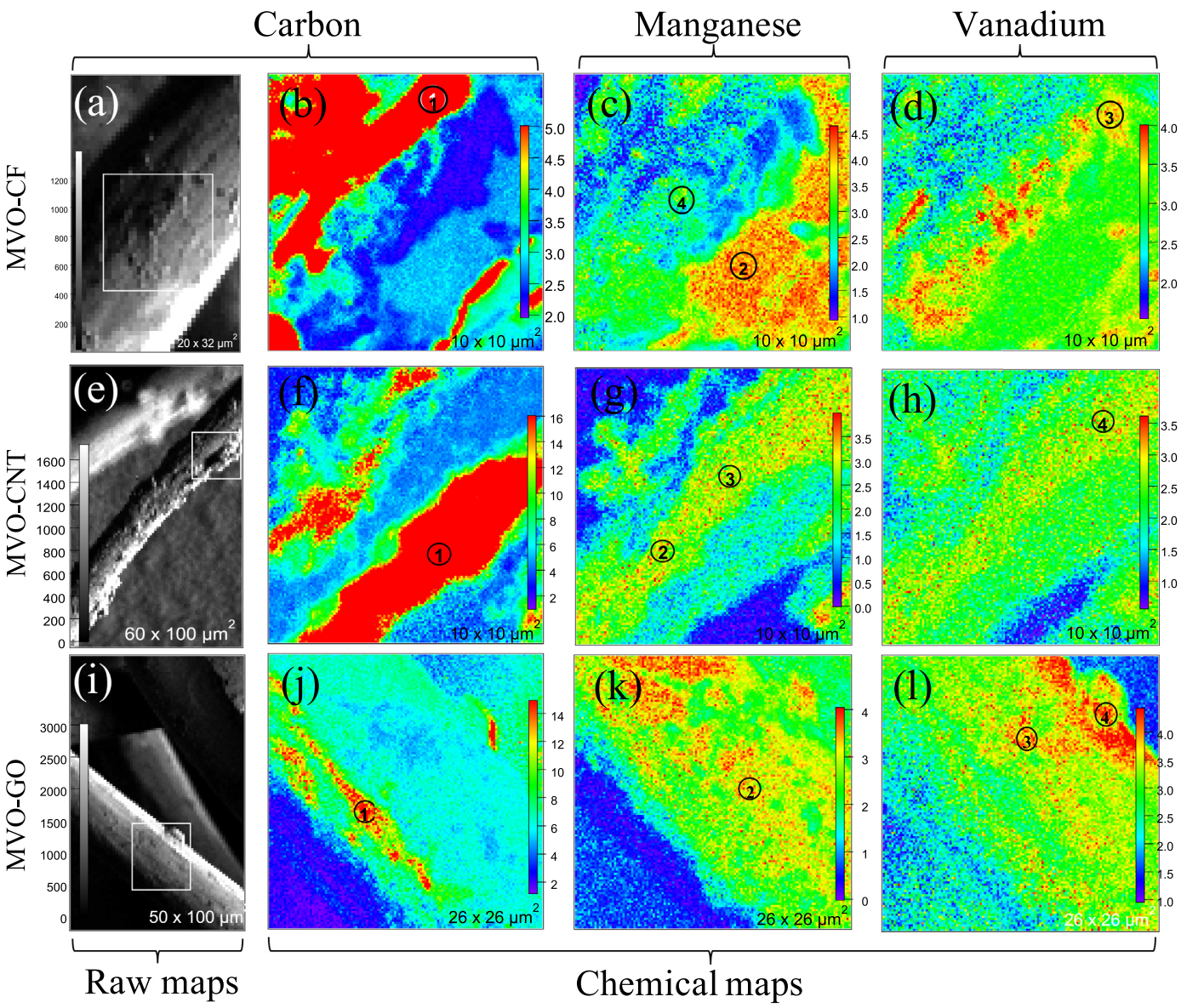

Fig. 4. Scanning photoemission microscope (SPEM) images acquired at pass energy of 40 eV. Where the first column shows topographic large area maps (raw maps) of carbon (C1s, BE = 283.8 eV), and second, third and fourth columns are representing the enlarged chemical SPEM maps at selected area as drawn by square in first column maps, of carbon, manganese (Mn3p, BE= 47.8 eV) and vanadium (V2p, BE = 515.8 eV) maps, of MVO-CF (a-d), MVO-CNT (e-h) and MVO-GO (i-l) samples, respectively.

agreement with regions observed in Raman spectra of this sample. On the other hand, MVO-CNT (Fig. 4e-h) as well as MVO-GO sample (Fig. 4i-l), show comparatively more uniform distribution of manganese and vanadium concentrations on the surface than MVO-CF sample where nanocarbon networks were absent. This indicates a more uniform distribution of the MVO phases on the surface of samples. Furthermore, the MVO-CNT and MVO-GO samples show a more homogeneous distribution and coverage of Mn and V phases with more density of coexisting $Mn_xV_2O_5$ in the former and dominance of manganese oxide in the later. In these two samples, the strong carbon signals are due to the intermixed CNTs and eGO structure with MVO on the surface.

To prepare a detailed electronic structural phase analysis of MVO phase distribution on the samples surface, the high-resolution C1s, Mn3p, O1s, and V2p core-level X-ray photoelectrons spectroscopy (XPS) spectra (Fig. 5) were acquired at defined pixels/points as marked on the SPEM maps shown in Fig. 4. In the C1s spectra (first column, Fig. 5), the samples show a principal component at ~ 284.5 ± 0.1 eV assigned to the carbonaceous components with broadening and slight shifts that can be assigned to the defective hexagonal rings, C-C sp^2, sp^2/sp^3 C-C bonds and adsorbed or lattice oxygen C-O/C-O-C bonds [27,43–46]. These C-C defects may be attributed to breaking of C-C bonds symmetry or carbon vacancies or replacements of carbon atoms from the C-C hexagonal ring. Furthermore, in C1s spectra of MVO-GO sample shows an additional components at ~ 282.5 ± 0.3 eV that can be associated to vanadium-carbon (V-C) bonds [38,47–49]. The deconvolution of C1s peak and BEs assignment for all three samples are shown in Fig.S1a in supporting information. On the other hand, the Mn3p spectra (second column, Fig. 5) of the samples show broad line shape with possible multiple components at BEs of ~ 47.5 ± 0.1, 48.4 ± 0.1, 49.1 ± 0.1, 49.9 ± 0.1, and 51.3 ± 0.1 eV that can be assigned to Mn^{2+} Mn^{3+} oxidation states in agreement with the formation of the MVO and manganese oxide in all samples [50,51]. In the O1s spectra, the components at ~ 530.6 ± 0.1, 530.8 ± 0.1, 531.7 ± 0.1 and 532.5 ± 0.1 eV are assigned to metal-oxygen (Mn-O), MVO, C-O and O-H bonds, respectively. The detailed O1s peak deconvolution is shown in Fig.S1b in supporting information. The

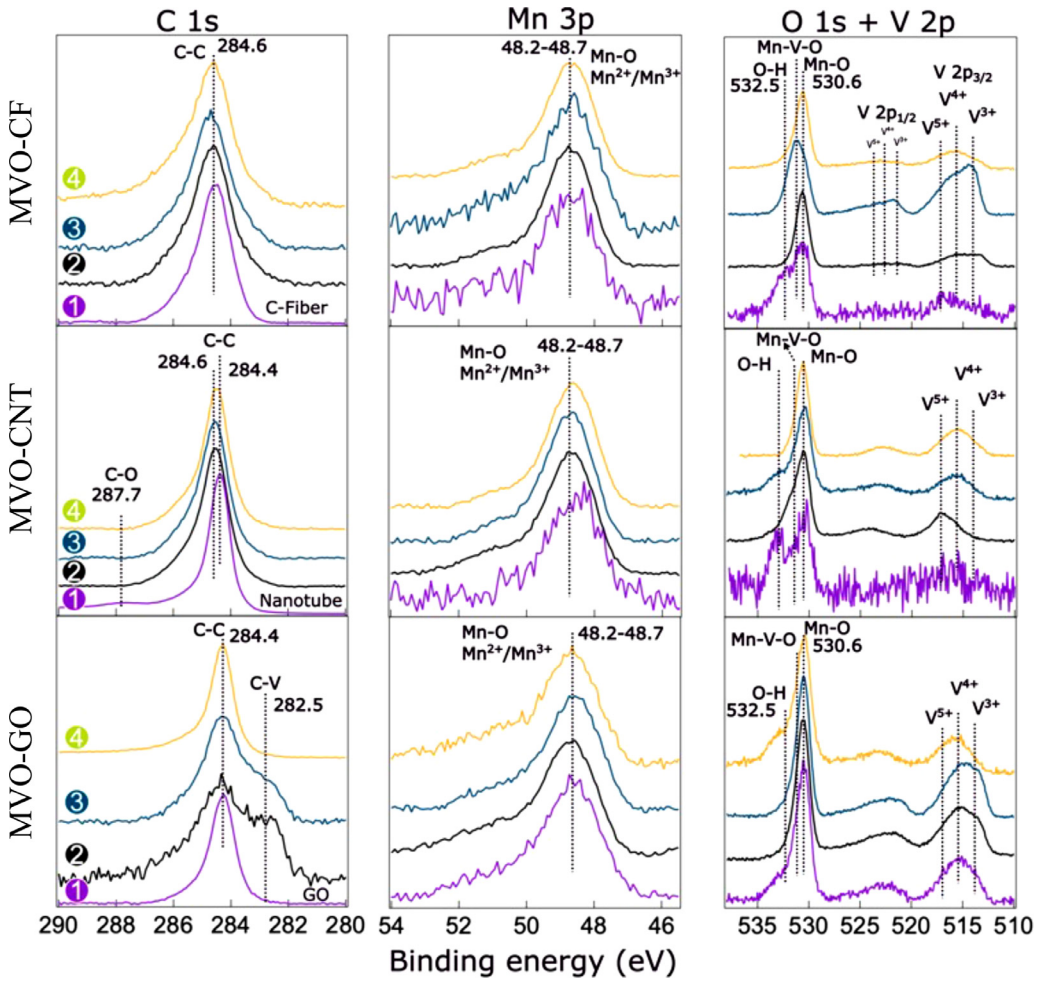

Fig. 5. High resolution XPS spectra of C1s; first column, Mn3p; second column and O1s+V2p; third column of MVO-CF (first row), MVO-CNT (second row), and MVO-GO (third row) samples. The spectra are acquired at the points marked by numbers on the SPEM maps of Fig. 4.

MVO phase showed a higher BE of 0.6 ± 0.1 eV than the manganese oxide phase in O1s core level spectra. This happens due to that in MVO phase the vanadium atoms are surrounded by manganese oxygen atoms which completely changes the coordination chemistry of MVO. Finally, the mixed vanadium oxidation states of V^{3+}, V^{4+} and V^{5+} were identified at BEs of 513.3 ± 0.5, 515.0 ± 0.5 and 517.0 ± 0.5 eV from $V2p_{3/2}$ core-level lines [49,52]. The MVO-CF sample shows a random distribution of the vanadium phases at different points on the sample, which is also in agreement with the Raman spectroscopy results. The MVO-CNT sample shows domination of the V^{4+} and V^{5+} consistent with the formation of the MVO and $Mn_xV_2O_5$ phases with higher concentration of the MVO formation at some points. On the other hand, the MVO-GO shows similar distribution with the domination of the sub-oxides such as $Mn_xV_2O_5$ and vanadium carbide (V-C bonds) with V^{3+} component contribution.

4. Discussions and conclusion

From the detailed morphological and structural phase analysis discussed in the previous sections, the carbon fiber without CNTs or eGO networks shows a non-homogeneous MVO material growth and its phase distribution. On the other hand MVO-CNTs and MVO-GO show a homogeneous material coating and structural phase distribution. The MVO-CNT sample shows the formation of the manganese oxide (Mn_2O_3) rich β-MVO phase while the MVO-GO sample shows the presence of other manganese vanadium sub-oxides ($Mn_xV_2O_5$) as well as carbon incorporation with vanadium. The -OH functional groups available on the GO surface bonded with vanadium cations during the co-electrochemical deposition process and formed the vanadium carbide phase on MVO-GO surface at some regions. The enhancement of the phase stability and homogeneity in presence of the different carbon material networks can be related either to the their hydrophilic properties or their catalytic characteristic, specially within the electrochemical redox process. Both carbon nanotubes and graphene oxide can act as catalysts in electrochemical redox process that can target distinct bonds within the redox process. Hence, they can modify the velocity of the reaction as well as the final material phase product. The detailed HRTEM analysis of bare CNTs-CF and GO-CF samples confirmed the defective cup-stacked type carbon nanotubes (CSCNTs) and layered graphene with large inter-planar distances of 0.6 nm and 0.18 nm, respectively (Fig.S2, supporting information). The unique properties of CSCNTs and GO provided a suitable surface for electrochemical MVO deposition in an aqueous electrolyte medium where the available functional groups interacted with metal oxide for the final material phase formation. Our results show the β- $Mn_2V_2O_7$ phase formation and conversion occurring in the presence of CNTs with dominance of MVO and Mn_2O_3 phase as indicated by an electrochemical reaction in previous section. In MVO-GO sample, the presence of electrolytic eGO shows dominance of uniform β-MVO phase without any presence of manganese oxide phase like in MVO-CNTs and MVO-CF samples which can be the result of either slower reaction or a different

bond target. Furthermore the crystalline structure of such network can also act a seed of the atomic redistribution of the MVO atoms in an ordered manner, which occurs within the CNTs hexagonal wall networks. However, GO shows the tendency for the vanadium incorporation which can deform the hexagonal network during co-electrodeposition process with $VOSO_4.xH_2O$ for the formation of $V_2O_5.nH_2O$ phase. This can be due to the higher density of defective C-C rings providing the chemical bonds with V^+ cations available in $VOSO_4.xH_2O$ electrolyte at applied potential value [53]. Hence, the eGO is expected to occur in sheets, as reported in previous literature [54], the final product is the formation of the GO nano-balls with MVO incorporation. The diverse phase distribution on the MVO-CNTs and MVO-GO can be related to the level of the hydrophilicity, the possible catalytic target of the functional hexagonal network (e.g., O-H or C-O groups) and the defect density of the grown nanocarbon network. The nanocarbon materials (CNTs, eGO) can do galvanic coupling resulting the superior capacity. However, MVO-CNTs and MVO-GO on carbon fibers in battery application requires a detailed study about the metal oxide and CNTs or GO concentration (i.e. weight percentage), which can regulate the electrical resistance of electrode. Then the performance of the constituent is drastically damaged. Additionally the exist work about β $Mn_2V_2O_7$ showed a good performance for Li-ion batteries [55]. Our results indicate that use of the these kind of carbon networks can significantly enhance the particular electrochemically grown MVO phase formation with uniform distribution. The β-MVO with Mn_2O_3 rich phase can play an important role in energy storage or hydrogen production mechanism where the MVO, Mn_2O_3 and CNTs may show a synergetic effect to improve the overall device performance. The addition of CNTs, eGO with MVO can improve electrical conductivity between metallic current collector and electrode in binder-free multi-cation batteries or super-capacitors application. Though, further investigations are required in order to clarify the fundamental mechanism behind the defective phase formation and distribution.

Declaration of Competing Interest

The authors declare that they have no known competing financial interests or personal relationships that could have appeared to influence the work reported in this paper.

Acknowledgement

R. Parmar thanks Elettra-Sincrotrone Trieste S.C.p.A. for postdoctoral fellowship. J. M. Rosolen (JMR) thanks to National Council of Scientific and Technological Development CNPq (307328/2017-1) and Fundação de Amparo á Pesquisa do Estado de São Paulo FAPESP (project 2017/04759-2) for funding in electrochemical experiments research. PR acknowledges the receipt of a fellowship from the ICTP programme for training and research in Italian laboratories, Trieste, Italy. M.K.T., G.H., and M.K. greatly acknowledge support from Czech Science Foundation, Czechia, project no. 20-08633X.

Supplementary materials

Supplementary material associated with this article can be found, in the online version, at doi:10.1016/j.cartre.2022.100218.

References

[1] A. D'Elia, S.J. Rezvani, N. Zema, F. Zuccaro, M. Fanetti, B. Belec, B.W. Li, C.W. Zou, C. Spezzani, M. Sacchi, A. Marcelli, M. Coreno, Stoichiometry and disorder influence over electronic structure in nanostructured VO_x films, J. Nanopart. Res. 23 (1) (2021) 33, doi:10.1007/s11051-020-05130-z.

[2] A. D'Elia, C. Grazioli, A. Cossaro, B.W. Li, C.W. Zou, S.J. Rezvani, N. Pinto, A. Marcelli, M. Coreno, Strain mediated filling control nature of the metal-Insulator transition of VO_2 and electron correlation effects in nanostructured films, Appl Surf Sci 540 (2021) 148341, doi:10.1016/j.apsusc.2020.148341.

[3] D. Cheng, Y. Li, J. Zhang, M. Tian, B. Wang, Z. He, L. Dai, L. Wang, Recent advances in electrospun carbon fiber electrode for vanadium redox flow battery: properties, structures, and perspectives, Carbon N Y 170 (2020) 527–542, doi:10.1016/j.carbon.2020.08.058.

[4] J. Sun, Y. Liu, H. Jiang, X. Dong, T. Hu, C. Meng, Y. Zhang, Mn^{2+} as the æspearheadg preventing the trap of Zn^{2+} in layered Mn^{2+} inserted hydrated vanadium pentoxide enables high rate capacity, J Colloid Interface Sci 602 (2021) 14–22, doi:10.1016/j.jcis.2021.05.163.

[5] R. Parmar, D.B. de Freitas Neto, E.Y. Matsubara, R. Gunnella, J.M. Rosolen, Electro-insertion of Mn^{2+} ions into $V_2O_5.nH_2O$ on MWCNTs coated carbon felt for binder-free Na^+ ion battery electrodes, Sustainable Energy Fuels 4 (2020) 3951–3962, doi:10.1039/D0SE00571A.

[6] Y. Li, D. Zhang, S. Huang, H.Y. Yang, Guest-species-incorporation in manganese/vanadium-based oxides: towards high performance aqueous zinc-ion batteries, Nano Energy 85 (2021) 105969, doi:10.1016/j.nanoen.2021.105969.

[7] S. Bi, S. Wang, F. Yue, Z. Tie, Z. Niu, A rechargeable aqueous manganese-ion battery based on intercalation chemistry, Nat. Commun. 12 (1) (2021) 1–11, doi:10.1038/s41467-021-27313-5.

[8] P. Luo, G. Liu, Z. Huang, C. Liu, P. Zhang, Y. Xiao, W. Tang, W. Zhang, H. Tang, S. Dong, Oxygen vacancy engineering boosted manganese vanadate toward high stability aqueous zinc ion batteries, J. Alloys Compd. (2022) 165804, doi:10.1016/j.jallcom.2022.165804.

[9] B.N.V. Krishna, S. Kammari, J.S. Yu, $Mn_2V_2O_7$ spiked ball-like material as bifunctional oxygen catalyst for zinc-air batteries, Int. J. Energy Res. (May 2022), doi:10.1002/er.8072.

[10] S. Gull, S.-C. Huang, C.-S. Ni, S.-F. Liu, W.-H. Lin, H.-Y. Chen, Operando synchrotron X-ray studies of MnVOH@SWCNT nanocomposites as cathodes for high-performance aqueous zinc-ion batteries, J. Mater. Chem. A 10 (2022) 14540–14554, doi:10.1039/D2TA02734H.

[11] X. Dong, Y. Zhang, C. Cui, S. Zeng, C. Fu, L. Wang, Study on the binary transition metal oxide $Mn_2V_2O_7$ structures for high performance lithium-ion batteries, J Alloys Compd 907 (2022) 164518, doi:10.1016/j.jallcom.2022.164518.

[12] Q. Sun, H. Cheng, W. Nie, X. Lu, H. Zhao, A comprehensive understanding of interlayer engineering in layered manganese and vanadium cathodes for aqueous Zn-Ion batteries, Chem. Asian J. 17 (7) (2022) e202200067, doi:10.1002/asia.202200067.

[13] B. Aslen, S. Koçak, Preparation of mixed-valent manganese-vanadium oxide and au nanoparticle modified graphene oxide nanosheets electrodes for the simultaneous determination of hydrazine and nitrite, J. Electroanal. Chem. 904 (2022) 115875, doi:10.1016/j.jelechem.2021.115875.

[14] M. Mondal, D.K. Goswami, T.K. Bhattacharyya, Microwave synthesized manganese vanadium oxide: high performing electrode material for energy storage, Mater. Today:. Proc. 50 (2022) 74–80, doi:10.1016/j.matpr.2021.04.155. International Virtual Conference on Advanced Nanomaterials and Applications (VCAN)

[15] T. Liu, L. Li, B. Liu, T. Yao, H. Wang, Polyvinylpyrrolidone-regulated synthesis of hollow manganese vanadium oxide microspheres as a high-performance anode for lithium-ion batteries, J. Colloid Interface Sci. 620 (2022) 144–152, doi:10.1016/j.jcis.2022.03.120.

[16] Q.A. Sial, S.S. Kalanur, H. Seo, Lamellar flower inspired hierarchical alpha manganese vanadate microflowers for high-performance flexible hybrid supercapacitors, Ceram. Int. (2022), doi:10.1016/j.ceramint.2022.05.152.

[17] Z. He, Y. Ueda, M. Itoh, Martensitic-like transition in $mn_2v_2o_7$ single crystals, Solid State Commun 147 (3) (2008) 138–140, doi:10.1016/j.ssc.2008.04.038.

[18] T.I. Krasnenko, M.V. Rotermel, Structural modification of $Mn_2V_2O_7$: Thermal expansion and solid solutions, Russ. J. Gen. Chem. 83 (9) (2013) 1640–1644, doi:10.1134/S1070363213090028.

[19] Q. Yan, G. Li, P.F. Newhouse, J. Yu, K.A. Persson, J.M. Gregoire, J.B. Neaton, $Mn_2V_2O_7$: an earth abundant light absorber for solar water splitting, Adv Energy Mater 5 (8) (2015) 1401840, doi:10.1002/aenm.201401840.

[20] D.B. Freitas Neto, F.F.S. Xavier, E.Y. Matsubara, R. Parmar, R. Gunnella, J.M. Rosolen, The role of nanoparticle concentration and CNT coating in high-performance polymer-free micro/nanostructured carbon nanotube-nanoparticle composite electrode for li intercalation, J. Electroanal. Chem. 858 (2020) 113826, doi:10.1016/j.jelechem.2020.113826.

[21] D.B. de Freitas Neto, R. Parmar, E.Y. Matsubara, M. Minicucci, R. Gunnella, J.M. Rosolen, Nanostructured $V_2O_5.nH_2O$/cup-stacked carbon nanotube composite with remarkable li+ specific capacity, Solid State Ionics 363 (2021) 115590, doi:10.1016/j.ssi.2021.115590.

[22] P. Asen, S. Shahrokhian, A.I. zad, One step electrodeposition of V_2O_5/polypyrrole/graphene oxide ternary nanocomposite for preparation of a high performance supercapacitor, Int J Hydrogen Energy 42 (33) (2017) 21073–21085, doi:10.1016/j.ijhydene.2017.07.008.

[23] G. Du, S.K. Hau, Z. Guo, J. Liu, W. Li, D. Jia, C. Cook, Z. Liu, H. Liu, Graphene$V_2O_5.nH_2O$ xerogel composite cathodes for lithium ion batteries, RSC Adv. 1 (2011) 690–697, doi:10.1039/C1RA00258A.

[24] T.X. Huong Le, M. Bechelany, M. Cretin, Carbon felt based-electrodes for energy and environmental applications: a review, Carbon N Y 122 (2017) 564–591, doi:10.1016/j.carbon.2017.06.078.

[25] A. Zhou, J. Bai, W. Hong, H. Bai, Electrochemically reduced graphene oxide: preparation, composites, and applications, Carbon N Y 191 (2022) 301–332, doi:10.1016/j.carbon.2022.01.056.
[26] B.D.L. Campéon, M. Akada, M.S. Ahmad, Y. Nishikawa, K. Gotoh, Y. Nishina, Non-destructive, uniform, and scalable electrochemical functionalization and exfoliation of graphite, Carbon N Y 158 (2020) 356–363, doi:10.1016/j.carbon.2019.10.085.
[27] Q. Liu, T. Fujigaya, N. Nakashima, Graphene unrolled from cup-stacked carbon nanotubes, Carbon N Y 50 (15) (2012) 5421–5428, doi:10.1016/j.carbon.2012.07.028.
[28] A. Bachmatiuk, F. Börrnert, F. Schäffel, M. Zaka, G.S. Martynkowa, D. Placha, R. Schönfelder, P.M.F.J. Costa, N. Ioannides, J.H. Warner, R. Klingeler, B. Büchner, M.H. Rümmeli, The formation of stacked-cup carbon nanotubes using chemical vapor deposition from ethanol over silica, Carbon N Y 48 (11) (2010) 3175–3181, doi:10.1016/j.carbon.2010.04.055.
[29] C.C. Zhou, F.M. Liu, D. Peng, L.g. Cai, W.w. Zhong, Molten salt synthesis and characterization of large size β-$Mn_2V_2O_7$ with single crystal character, J Alloys Compd 505 (2) (2010) 573–578, doi:10.1016/j.jallcom.2010.06.075.
[30] L. Zhao, S. Lin, K. Bi, C. Liang, Y. Du, J. Liu, H. Yang, D. Fan, Y. Wang, M. Lei, Manganese vanadium oxide hollow microspheres: a novel electrocatalyst for oxygen reduction reaction, J. Solid State Electrochem. 6 (21) (2017) 1743–1749, doi:10.1007/s10008-017-3548-9.
[31] E. Dorm, B.O. Marinder, Thortveitite-type structure of $Mn_2V_2O_7$, Acta Chem Scand 21 (1967) 590–591.
[32] J.H. Liao, F. Leroux, C. Payen, D. Guyomard, Y. Pilfered, Synthesis, structures, magnetic properties, and phase transition of manganese(II) divanadate: $mn_2v_2o_7$, J Solid State Chem 121 (1996) 214–224.
[33] S.J. Rezvani, Y. Mijiti, A. Di Cicco, Porous silicon nanowires phase transformations at high temperatures and pressures, Appl Phys Lett 119 (5) (2021) 053101, doi:10.1063/5.0057706.
[34] H. Rahaman, R.M. Laha, D.K. Maiti, S.K. Ghosh, Fabrication of Mn_2O_3 nanorods: an efficient catalyst for selective transformation of alcohols to aldehydes, RSC Adv. 5 (2015) 33923–33929, doi:10.1039/C5RA02504D.
[35] X. Niu, H. Wei, K. Tang, W. Liu, G. Zhao, Y. Yang, Solvothermal synthesis of 1D nanostructured Mn_2O_3: effect of Ni^{2+} and Co^{2+} substitution on the catalytic activity of nanowires, RSC Adv. 5 (2015) 66271–66277, doi:10.1039/C5RA14618F.
[36] J.E. Post, D.A. McKeown, P.J. Heaney, Raman spectroscopy study of manganese oxides: tunnel structures, Am. Mineral. 105 (8) (2020) 1175–1190, doi:10.2138/am-2020-7390.
[37] C.T.J. Low, F.C. Walsh, M.H. Chakrabarti, M.A. Hashim, M.A. Hussain, Electrochemical approaches to the production of graphene flakes and their potential applications, Carbon N Y 54 (2013) 1–21, doi:10.1016/j.carbon.2012.11.030.
[38] P. Han, H. Wang, Z. Liu, X. Chen, W. Ma, J. Yao, Y. Zhu, G. Cui, Graphene oxide nanoplatelets as excellent electrochemical active materials for VO2+/VO2+ and V2+/V3+ redox couples for a vanadium redox flow battery, Carbon N Y 49 (2) (2011) 693–700, doi:10.1016/j.carbon.2010.10.022.
[39] R. Parmar, D.B. de Freitas Neto, E.Y. Matsubara, R. Gunnella, J.M. Rosolen, Electrochemical synthesis and structural characterization of nanostructured $v_2o_5.nh_2o$ on CNTs coated/uncoated carbon felt composite, Nano Structures & Nano Objects 24 (2020) 100538, doi:10.1016/j.nanoso.2020.100538.
[40] S.J. Rezvani, A. D'Elia, S. Macis, S. Nannarone, S. Lupi, F. Schütt, F. Rasch, R. Adelung, B. Lu, Z. Zhang, L. Qu, X. Feng, A.R. Vázquez, A. Marcelli, Structural anisotropy in three dimensional macroporous graphene: a polarized XANES investigation, Diam Relat Mater 111 (2021) 108171, doi:10.1016/j.diamond.2020.108171.
[41] S.J. Rezvani, R. Parmar, F. Maroni, F. Nobili, A. Di Cicco, R. Gunnella, Does alumina coating alter the solid permeable interphase dynamics in limn2o4 cathodes? The Journal of Physical Chemistry C 124 (49) (2020) 26670–26677, doi:10.1021/acs.jpcc.0c08449.
[42] L. Gregoratti, A. Barinov, E. Benfatto, G. Cautero, C. Fava, P. Lacovig, D. Lonza, M. Kiskinova, R. Tommasini, S. Mähl, W. Heichler, 48-Channel electron detector for photoemission spectroscopy and microscopy, Rev. Sci. Instrum. 75 (1) (2004) 64–68, doi:10.1063/1.1630837.
[43] A. Barinov, O.B. Malciolu, S. Fabris, T. Sun, L. Gregoratti, M. Dalmiglio, M. Kiskinova, Initial stages of oxidation on graphitic surfaces: photoemission study and density functional theory calculations, J. Phys. Chem. C 113 (21) (2009) 9009–9013, doi:10.1021/jp902051d.
[44] G. Moraitis, Z. Åpitalský, F. Ravani, A. Siokou, C. Galiotis, Electrochemical oxidation of multi-wall carbon nanotubes, Carbon N Y 49 (8) (2011) 2702–2708, doi:10.1016/j.carbon.2011.02.060.
[45] A. Kovtun, D. Jones, S. Dell-Elce, E. Treossi, A. Liscio, V. Palermo, Accurate chemical analysis of oxygenated graphene-based materials using X-ray photoelectron spectroscopy, Carbon N Y 143 (2019) 268–275, doi:10.1016/j.carbon.2018.11.012.
[46] S.A. Chernyak, A.S. Ivanov, A.M. Podgornova, E.A. Arkhipova, S.Y. Kupreenko, A.V. Shumyantsev, N.E. Strokova, K.I. Maslakov, S.V. Savilov, V.V. Lunin, Kinetics of the defunctionalization of oxidized few-layer graphene nanoflakes, Phys. Chem. Chem. Phys. 20 (2018) 24117–24122, doi:10.1039/C8CP05149F.
[47] M.D. Antonik, R.J. Lad, T.M. Christensen, Clean surface and oxidation behavior of vanadium carbide, $VC_{0.75}$(100), Surf. Interface Anal. 24 (10) (1996) 681–686, doi:10.1002/(SICI)1096-9918(19960930)24:10<681::AID-SIA179>3.0.CO;2-T.
[48] J.-G. Choi, The surface properties of vanadium compounds by X-ray photoelectron spectroscopy, Appl Surf Sci 148 (1) (1999) 64–72, doi:10.1016/S0169-4332(99)00132-4.
[49] H. Li, P. Tang, H. Shen, T. Hu, J. Chen, K. Chen, F. Qi, H. Yang, L. Wen, F. Li, Scalable fabrication of vanadium carbide/graphene electrodes for high-energy and flexible microsupercapacitors, Carbon N Y 183 (2021) 840–849, doi:10.1016/j.carbon.2021.07.066.
[50] E.S. Ilton, J.E. Post, P.J. Heaney, F.T. Ling, S.N. Kerisit, XPS determination of Mn oxidation states in Mn(hydr)oxides, Appl. Surf. Sci. 366 (2016) 475–485, doi:10.1016/j.apsusc.2015.12.159.
[51] M. Oku, K. Hirokawa, S. Ikeda, X-ray photoelectron spectroscopy of manganeseoxygen systems, J. Electron Spectrosc. Relat. Phenom. 7 (5) (1975) 465–473, doi:10.1016/0368-2048(75)85010-9.
[52] E. Hryha, E. Rutqvist, L. Nyborg, Stoichiometric vanadium oxides studied by XPS, Surf. Interface Anal. 44 (8) (2012) 1022–1025, doi:10.1002/sia.3844.
[53] Y. Sun, X. Tang, H. Bao, Z. Yang, F. Ma, The effects of hydroxide and epoxide functional groups on the mechanical properties of graphene oxide and its failure mechanism by molecular dynamics simulations, RSC Adv. 10 (49) (2020) 29610–29617, doi:10.1039/D0RA04881J.
[54] J. Chen, M. Perez-Page, Z. Ji, Z. Zhang, Z. Guo, S. Holmes, One step electrochemical exfoliation of natural graphite flakes into graphene oxide for polybenzimidazole composite membranes giving enhanced performance in high temperature fuel cells, J. Power Sources 491 (2021) 229550, doi:10.1016/j.jpowsour.2021.229550.
[55] D. Xia, S. Xu, W. Wang, D. Wang, M. Wu, F. Gong, Pure-phase β-$Mn_2V_2O_7$ interconnected nanospheres as a high-performance lithium ion battery anode, Chem. Commun. 56 (2020) 8043–8046, doi:10.1039/D0CC02458A.